CaH_2. Sample concentrations were on the order of 10^{-4} M. Solvent was degassed by using four freeze-pump-thaw cycles.

X-ray Data Collection for $[Ir(CNCH_3)_2Au(\mu\text{-dpm})_2](PF_6)_2 \cdot CH_2Cl_2$. The blocklike crystals were formed by slow diffusion of 2-propanol into a methylene chloride solution of $[Ir(CNCH_3)_2Au(\mu\text{-dpm})_2](PF_6)_2$. To prevent cracking, the crystal was coated with light hydrocarbon oil. The crystal was mounted on a glass fiber with silicon grease and placed into the 130 K nitrogen stream of a Syntex $P2_1$ diffractometer with a modified LT-1 low-temperature apparatus. Unit cell parameters were determined by least-squares refinement of 10 reflections with $10.8 < 2\theta < 16.8°$. The parameters were verified by examination of axial photos. This refinement yielded the monoclinic crystal system. The unique space group $P2_1/c$ (No. 14) was determined by the following conditions: $h00$, $h = 2n$; $0k0$, $k = 2n$; $00l$, $l = 2n$. The two check reflections remained stable throughout the data collection. The data were corrected for Lorentz and polarization effects. Crystal data are given in Table IV. Scattering factors and corrections for anomalous dispersion were taken from a standard source.[27]

Solution and Structure Refinement for $[Ir(CNCH_3)_2Au(\mu\text{-dpm})_2](PF_6)_2 \cdot CH_2Cl_2$. Calculations were performed on a Data General MW/10000 computer. The structure was solved in the centrosymmetric space group $P2_1/c$ (No. 14), and heavy atom positions for Ir and Au were assigned via the Patterson function. All non-carbon atoms and the isocyanide carbons, C(1) to C(4), were refined with anisotropic thermal parameters, while all others were left isotropic. Hydrogens were fixed to all carbons where chemically justified, except the solvent carbon, C(55). The hydrogen atom positions were calculated by using a riding model with C-H vector fixed at 0.96 Å and a thermal parameter 1.2 times the host carbon. The largest unassigned peak in the final difference map had density equal to 1.65 e/Å^3. This peak is 1.38 Å from C(12). Absorption corrections were applied,[28] and the structure was refined to convergence. The goodness of fit was calculated at 1.076 with a mean (shift/esd) of 0.010 for the overall scale.

X-ray Data Collection for $[Ir(CNCH_3)_3Au(\mu\text{-dpm})_2](PF_6)_2$. The blocklike crystals were formed by slow diffusion of diethyl ether into a methylene chloride solution of $[Ir(CNCH_3)_3Au(\mu\text{-dpm})_2](PF_6)_2$. To prevent cracking, the crystal was coated with light hydrocarbon oil. The crystal was handled as described above. Unit cell parameters were determined by least-squares refinement of 12 reflections with $27.2 < 2\theta < 31.2°$. The parameters were verified by examination of axial photos. This refinement yielded the monoclinic crystal system. The unique space group $C2/c$ (No. 15) was determined by the conditions hkl, $h + k = 2n$ and $l = 2n$. The two check reflections remained stable throughout the data collection. The data were corrected for Lorentz and polarization effects. Crystal data are given in Table IV.

Solution and Structure Refinement for $[Ir(CNCH_3)_3Au(\mu\text{-dpm})_2](PF_6)_2$. Calculations were performed on a Data General MV/10000 computer. The structure was solved in the centrosymmetric space group $C2/c$, and heavy atom positions (Ir and Au) were assigned via the Patterson function. All non-carbon atoms and the methyl isocyanide carbon atoms were refined with anisotropic thermal parameters, while all others were left isotropic. Hydrogens were treated as described above. Large thermal motion is seen in the terminal carbon (C(6)) of the methyl isocyanide trans to Au(1). To verify assignment as a single methyl group and not a disordered unit, the address was removed, and the structure was refined. Subsequent inspection of a Fourier difference map produced only one peak in the same location, thus verifying the assignment. The largest unassigned peak in the final difference map had density equal to 2.91 e/Å^3. This peak is 1.26 Å from Au(1). Absorption corrections were applied, and the structure was refined to convergence. The goodness of fit was calculated at 1.697 with a mean (shift/esd) of 0.010 for the overall scale.

Acknowledgment. We thank the National Science Foundation (Grant CHE-8941209) for support, Johnson-Matthey, Inc., for a loan of iridium salts, Professor P. B. Kelly for assistance in measuring the emission lifetimes, and Dr. Marilyn Olmstead, B. Noll, and E. Fung for crystallographic assistance.

Supplementary Material Available: Tables of atomic positional parameters, bond distances, bond angles, anisotropic thermal parameters, and hydrogen atom positions for **2** and **3** (10 pages); listings of structure factors for **2** and **3** (53 pages). Ordering information is given on any current masthead page.

(26) Balch, A. L.; Catalano, V. J.; Olmstead, M. M. *J. Am. Chem. Soc.* **1990**, *112*, 7558.
(27) *International Tables for X-ray Crystallography*; Kynoch: Birmingham, England, 1974; Vol. 4.
(28) The method obtains an empirical tensor from an expression relating F_o and F_c: Moezzi, B. Ph.D. Thesis, University of California, Davis, 1987.

Contribution from the Departments of Chemistry, Princeton University, Princeton, New Jersey 08544, and Colorado State University, Fort Collins, Colorado 80523

Analysis of a Siroheme Model Compound: Core-Size Dependence of Resonance Raman Bands and the Siroheme Spin State in Sulfite Reductase

Dan Melamed,[†] Eric P. Sullivan, Jr.,[‡] Kristine Prendergast,[†] Steven H. Strauss,[‡] and Thomas G. Spiro*,[†]

Received July 27, 1990

Resonance Raman (RR) and infrared spectra are reported for nickel(II) octaethylisobacteriochlorin (OEiBC) and its $^{15}N_4$ and *meso*-d_2 isotopomers. The bands are assigned to porphyrin-like modes with the aid of a normal-coordinate analysis by using a force field developed for nickel octaethylporphyrin (OEP) and by scaling the force constants to bond lengths expected on the basis of the crystal structure of nickel *meso*-tetramethylisobacteriochlorin. The eigenvectors show a relationship between OEP and OEiBC modes, despite some localization to one or the other half of the OEiBC ring caused by the unequal lengths of the methine bridge bonds adjacent to the pyrrole and pyrroline rings. Excitation at wavelengths near the B and Q absorption bands show Q-resonant RR spectra to be dominated by a single Franck-Condon active mode, ν_{29}, for NiOEiBC, in contrast to the vibronic scattering from many modes seen in porphyrins. On the other hand, B-resonant spectra that are dominated by Franck-Condon active modes for porphyrins show equally strong enhancement of vibronic modes in NiOEiBC. These differences are attributed to the energy separation of the a_{1u} and a_{2u} HOMO's, brought about by pyrrole ring reduction, and the resultant diminution of effects which are associated with configuration interaction. When the vibrational assignments are used to track the RR bands of a series of iron-OEiBC complexes, a distinctive dependence of the high-frequency bands on the ring core size of the porphyrin analogues is observed, although the slopes of the correlations differ from those reported previously for porphyrin or chlorin. Direct comparison of the iron-OEiBC high-frequency bands with those of the *Escherichia coli* sulfite reductase hemoprotein confirms the previous inference that the iron(II) siroheme is intermediate spin in the semireduced protein but high spin in the fully reduced protein.

Introduction

Resonance Raman (RR) spectroscopy, a well-established technique for studying structure and dynamics in metalloporphyrins and heme proteins,[1] is increasingly being extended to reduced porphyrins,[2-6] especially in connection with the structural analysis of chlorophyll and chlorin-containing proteins. Although

* Author to whom correspondence should be addressed.
[†] Princeton University.
[‡] Colorado State University.

(1) Spiro, T. G.; Li, X. Y. In *Biological Applications of Raman Spectroscopy*; John Wiley: New York, 1988; Vol. II.
(2) Schick, G. A.; Bocian, D. F. *Biochim. Biophys. Acta* **1987**, *895*, 127.
(3) Andersson, L. A.; Loehr, T. M.; Stershic, M. T.; Stolzenberg, A. M. *Inorg. Chem.* **1990**, *29*, 2278.
(4) Kitagawa, T.; Ozaki, Y. *Struct. Bonding (Berlin)* **1987**, *64*, 1.

0020-1669/91/1330-1308$02.50/0

pyrrole ring reduction has pronounced effects on the electronic spectrum, systematic examination of metallochlorin RR spectra have suggested marked parallelism of the vibrational modes with those of metalloporphyrins, extending to the observation of a systematic dependence of skeletal mode frequencies on the ring core size for both macrocycles.[4,5] This parallelism has recently been confirmed with a normal-coordinate analysis of nickel(II) octaethylchlorin (OEC)[7] using a force field developed for nickel(II) octaethylporphyrin (OEP),[8] with proper scaling of the force constants to accommodate bond distance variations due to the pyrrole ring reduction. This analysis provided a satisfactory account of the RR frequencies and isotope shifts, as well as the polarizations and enhancement patterns. The calculated eigenvectors showed a high degree of isomorphism for many chlorin and porphyrin modes, in contrast to an earlier report of a semiempirical QCFF/π calculation, which had led to the conclusion that mode localization in chlorin obscures the correspondences with porphyrin.[9] This conclusion is not borne out by the calculations with the empirically adapted valence force field.

Reduction of two adjacent pyrrole rings transforms porphyrin to isobacteriochlorin, the macrocycle found in siroheme-containing proteins; the prototype is sulfite reductase[10] (SiR), from which siroheme derives its name. SiR catalyzes the six-electron reduction of sulfite to hydrogen sulfide or of nitrite to ammonia. It contains an Fe_4S_4 cluster in addition to the siroheme; Mössbauer[11] and EPR[12] spectroscopy show the two metal centers to be coupled magnetically. A model of the site, involving a bridging cysteine ligand between the siroheme Fe and one of the cluster Fe atoms, is consistent with the X-ray crystal structure of SiR from *Escherichia coli*.[13] RR spectroscopy of this protein showed selective enhancement of cluster[14] as well as siroheme modes when the laser wavelength was tuned to the appropriate electronic transition. The high-frequency siroheme modes showed redox-associated shifts that were reminiscent of those known to accompany spin and oxidation state changes in iron porphyrins. These shifts, when taken in conjunction with previous Mossbauer measurements, led to the tentative conclusion that one-electron reduction of oxidized SiR produces iron(II) siroheme, which is in an intermediate spin state,[15] while addition of a second electron, which reduces the cluster, converts the iron(II) siroheme to a high-spin state. Because this behavior implies a significant dependence of the siroheme axial ligation on the cluster redox level and therefore has implications for the enzyme mechanism, it is clearly of interest to put the interpretation of the RR spectra on a firmer basis.

To this end, we have studied RR spectra of metallooctaethylisobacteriochlorins (OEiBC's) and have carried out a normal coordinate analysis of NiOEiBC, for which infrared spectra and ^{15}N and *meso*-d_3 isotope shifts have also been collected. Again, the NiOEP force field was used, with scaling of the force constants to accommodate bond distance changes, inferred from the crystal structure of nickel *meso*-tetramethylisobacteriochlorin (TMiBC).[16] The analysis shows that the iBC modes retain some memory of their OEP parentage as gauged by the eigenvectors, although there is significant localization to the reduced or oxidized half of the iBC ring, associated with differences in the methine bond lengths. Consistent with this memory, the metallo-OEiBC frequencies are correlated with core size as judged from the structures of porphyrin analogues, although the slopes of the correlations differ from those of metallo-OEP's. The availability of RR spectra for OEiBC, containing Fe(III) and Fe(II) in the standard coordination and spin states, provides direct confirmation that the iron(II) siroheme is intermediate and high spin, respectively, in one- and two-electron-reduced SiR. Oxidized SiR appears to contain six- rather than five-coordinate high-spin Fe(III).

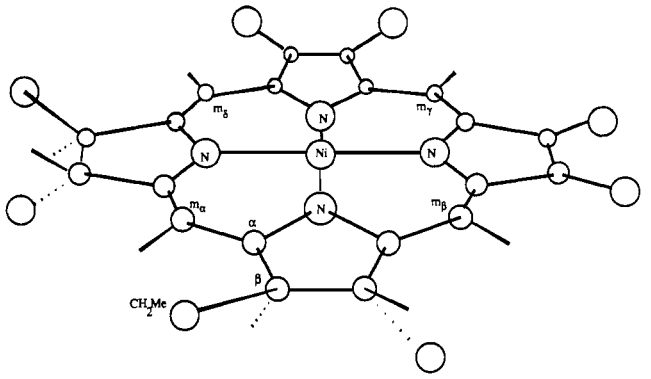

Figure 1. Structural diagram for the model of NiOEiBC used in the normal mode calculation. The numbering scheme for the ethyl groups (CH_2Me) in Tables IV and V is as follows: C_1 is the methylene position, and C_2 is the terminal point mass methyl.

The reduction of the pyrrole rings also has marked effects on the iBC absorption bands and the RR enhancement pattern. These changes can be understood in terms of porphyrin electronic structure, when the effect of the ring reduction on the orbital interactions is taken into account.

Experimental Section

H_2OEiBC was prepared by literature methods.[17] Fe^{II}OEiBC was prepared by metalation of the free base in THF with $FeBr_2$. Upon completion of the reaction, all solvent was removed under vacuum, and the product was extracted with hexane and filtered through Celite. The hexane was removed and the compound dissolved in benzene. In those cases where ligated complexes were studied, a 0.1 M benzene solution of the appropriate base was used. Special care was taken to avoid using dichloromethane, since it has been shown to oxidize ferrous isobacteriochlorins.[18] Ni^{II}OEiBC was prepared as above, by using $Ni(OAc)_2 \cdot 4H_2O$ and methanol. [Fe^{III}OEiBC]Cl was prepared by bubbling 1 mL of a mixture of air and HCl vapor through a benzene solution of Fe^{II}OEiBC and then removing solvent under vacuum. The $[Fe^{III}OEiBC(DMSO)_2]^+$ was obtained by dissolving [Fe^{III}OEiBC]Cl in DMSO. $[Fe^{III}OEiBC(N\text{-MeIm})_2]^+$ was prepared by adding *N*-methylimidazole to the aforementioned DMSO solution.

The ^{15}N labeled compound was synthesized from the analogous ^{15}N-OEP compound which was prepared as described in the literature.[19] *meso*-OEiBC-d_3 was obtained via exchange of the free base with trifluoroacetic acid-*d*.[20] The resultant free base was metalated with nickel and then assayed with ^1H NMR spectroscopy (General Electric QE300 FT NMR). The ^1H NMR spectrum of the Ni species in benzene-d_6 indicated a single resonance at 8.56 ppm integrating for a single proton at the γ-position. This is the least acidic position, and extreme conditions are required for its deuteration.[20]

Infrared spectra were recorded with a Nicolet 730 FTIR instrument, using samples pressed into KBr pellets. Absorption spectra were recorded on a Hewlett Packard 84451A diode array spectrophotometer, using a 2 mM anaerobic cell. Resonance Raman spectra were obtained on solution samples, as described previously,[21] or on solids in KBr pellets,

(5) Tasumi, F.; Fujiwara, M. *Adv. Spectrosc.* **1987**, *14*, 407.
(6) Lutz, M. In *Advances In Infrared and Raman Spectroscopy*; Clarke, R. J. H., Hester, R. E., Eds.; Wiley-Heyden: London, 1987; Vol. III, p 211.
(7) Prendergast, K.; Spiro, T. G. *J. Phys. Chem.*, in press.
(8) Li, X. Y.; Czernuszewicz, R. S.; Kincaid, J. R.; Stein, P.; Spiro, T. G. *J. Phys. Chem.* **1990**, *94*, 47.
(9) Boldt, N. J.; Donohoe, R. J.; Birge, R. R.; Bocian, D. F. *J. Am. Chem. Soc.* **1987**, *109*, 2284.
(10) Siegel, L. M.; Murphy, M. J.; Kaiser, H. J. *J. Biol. Chem.* **1973**, *248*, 251.
(11) Christner, J. A.; Munck, E.; Janik, P. A.; Siegel, L. M. *J. Biol. Chem.* **1981**, *256*, 2098.
(12) Janick, P. A.; Siegel, L. M. *Biochemistry* **1982**, *21*, 3538.
(13) McRee, D. E.; Richardson, D. C.; Richardson, J. S.; Siegel, L. M. *J. Biol. Chem.* **1986**, *261*, 10277.
(14) Han, S.; Madden, J. F.; Thompson, R. G.; Strauss, S. H.; Siegel, L. M.; Spiro, T. G. *Biochemistry* **1989**, *28*, 5461.
(15) Madden, J. F.; Han, S.; Siegel, L. M.; Spiro, T. G. *Biochem.* **1989**, *28*, 5471.
(16) Suh, M. P.; Swepston, P. N.; Ibers, J. A. *J. Am. Chem. Soc.* **1984**, *106*, 5164.
(17) Stolzenberg, A. M.; Spreer, L. O.; Holm, R. H. *J. Am. Chem. Soc.* **1980**, *102*, 364.
(18) Strauss, S. H.; Holm, R. H. *Inorg. Chem.* **1982**, *21*, 863.
(19) Paine, J. B.; Kirshner, W. B.; Maskowitz, D. W.; Dolphin, D. *J. Org. Chem.* **1976**, *41*, 3857.
(20) Bonnett, R.; Gale, I. A. D.; Stephenson, G. F. *J. Chem. Soc. C* **1967**, 1168.
(21) Czernuszewicz, R. S. *Appl. Spec.* **1986**, *40*, 571.

Table I. Averaged[a] Structural Parameters of NiTMiBC

	pyrroline rings	pyrrole rings		pyrroline rings	pyrrole rings
		Bonds (Å)			
αN[b]	1.378	1.382	mH[c]	1.098	1.098
$\alpha\beta$	1.499	1.412	β1	1.531	1.501
$\beta\beta$	1.508	1.343	NiN	1.926	1.916
αm[c]	1.355	1.397	12	1.526	1.526
		Angles (deg)			
$\alpha N\alpha$	108.3	105.6	Nαm	125.7	124.8
N$\alpha\beta$	110.7	109.3	m$\alpha\beta$	123.0	125.3
$\alpha\beta\beta$	103.5	107.7	αmα[d]		

[a] The two sides of the macrocycle related by the C_2 axes were averaged, as were the two independent molecules. [b] α, β, m, 1, and 2 refer to the five different types of carbon atoms labeled in Figure 1. [c] Bonds adjacent to the cited rings. [d] The values are 119.9, 122.2, and 121.8°, respectively, for angles between two pyrroline rings, between two pyrrole rings, and between one pyrrole and one pyrroline ring.

cooled to 10 K with a CSA-202E closed-cycle liquid He cryotip (Air Products, Allentown, PA). Laser excitation at 406 and 568 nm was provided by a Coherent Innova 100K3 Kr^+ ion laser, while 595-nm excitation was obtained by using a Coherent 590 tunable dye laser, pumping rhodamine 6G. The scattered light was dispersed with a Spex 1401 double monochromator, equipped with an RCA CC31034A photomultiplier tube.

Results and Discussion

1. Normal-Mode Analysis. Normal modes were calculated for the model of NiOEiBC shown in Figure 1. Structural parameters were taken from the X-ray crystal structure of nickel *meso*-tetramethylisobacteriochlorin (TMiBC),[16] the NiOEiBC structure being unavailable. Several other iBC structures have been reported;[22] the structural parameters are similar to those of NiTMiBC. In porphyrins, the effects of different substituents on the skeletal bond distances are known to be small. NiTMiBC is ruffled, but a planar macrocycle was employed in the model to avoid the difficulties of combining in- and out-of-plane force fields. Because ruffling is expected to influence the vibrational frequencies, an exact fit to the observed spectra is not expected. The planar approximation should not affect the forms of the normal modes, however. It is known that isotope shifts are essentially the same for ruffled and planar forms of NiOEP[23] despite appreciable frequency differences, implying that the eigenvectors are largely unaltered. As in the NiOEP and NiOEC calculation, the ethyl substituents were included as methylene groups with point mass methyl groups. The methyl groups were oriented out of the plane, pointing alternately up and down to maintain C_2 molecular symmetry. The pyrroline H atoms, which are trans to each other on a given ring, were likewise arranged to maintain C_2 symmetry, although both inter-ring isomers are present in the experimental sample. Isomer heterogeneity may be a source of band broadening and possibly of extra bands in spectral regions sensitive to ring substituents.

The structure parameters, given in Table I, were averaged to maintain C_2 symmetry for the macrocycle. As expected, the pyrroline rings have longer $C_\beta C_\beta$ and $C_\alpha C_\beta$ bonds than do the pyrrole rings. In addition, the $C_\alpha C_m$ bonds ajdacent to the pyrrole rings are seen to be 0.040 Å longer on average than those adjacent to the pyrroline rings. A similar bond length difference was found for FeOEC, used as a model in the NiOEC calculation.[7] However, the short and long $C_\alpha C_m$ bonds are arranged in an alternating pattern for chlorin, while in isobacteriochlorin the short and long bonds are segregated on separate halves of the molecule. It cannot be excluded, however, that this segregation is partly an artifact of the averaging procedure. For both independent molecules in the NiTMiBC unit cell, the ranges of the $C_\alpha C_m$ bond lengths on both sides of the macrocycles are greater than the 0.04-Å difference of the averages.[16] The general valence force field developed for NiOEP[8] was used as the starting point in the calculation of the normal-mode frequencies. As in the case of NiOEC, stretching force constants were initially scaled to the bond distances, using the equation of Burgi and Dunitz.[24] They were then adjusted slightly to improve the fit to the experimental frequencies. Angle bending and interaction force constants were carried over directly from NiOEP and NiOEC. The calculation was performed with the **GF** matrix method, using an updated version of Schachtschneider's programs,[25] implemented on a VAX-11/780 computer. The final force constants are listed in Tables II and III. Twnenty-one of them (indicated by asterisks) were adjusted, and the average error in the calculated frequencies was 16 cm^{-1} for 44 observed frequencies of the natural abundance species, while the average error for the 66 observed isotope shifts was 3 cm^{-1}.

Table II. Diagonal Force Constants for NiOEiBC[a]

internal coord	pyrroline rings	pyrrole rings
$\kappa(\alpha N)_1$	5.592*	5.557*
$K(\alpha\beta)_2$	4.890*	5.949*
$\kappa(\beta\beta)_3$	3.857*	6.800*
$\kappa(\alpha m)_4$	7.550*	6.300*
$\kappa(mH)_5$	4.560	4.560
$\kappa(\beta 1)_6$	3.689*	4.108
$\kappa(MN)_7$	1.813*	1.857*
$\kappa(12)_8$	4.600	4.600
$\kappa(1H)_9$	4.560	4.560
$\kappa(\beta H)_{10}$	4.560	4.560
$H(\alpha N\alpha)_{11}$	1.620	1.620
$H(N\alpha\beta)_{12}$	1.370	1.370
$H(\alpha\beta\beta)_{13}$	1.370	1.370
$H(MN\alpha)_{14}$	0.300	0.300
$H(N\alpha m)_{15}$	0.830	0.830
$H(m\alpha\beta)_{16}$	0.830	0.830
$H(\alpha m\alpha)_{17}$	1.100	1.100
$H(\alpha\beta 1)_{18}$	1.200	1.200
$H(\beta\beta 1)_{19}$	1.200	1.200
$H(\beta 12)_{20}$	1.200	1.200
$H(NMN)_{21}$	0.250	0.250
$H(\alpha mH)_{22}$	0.450	0.450
$H(\beta 1H)_{23}$	0.625	0.625
$H(21H)_{24}$	0.625	0.625
$H(H1H)_{25}$	0.540	0.540
$H(\alpha\beta H)_{26}$	0.400*	
$H(\beta\beta H)_{27}$	0.400*	
$H(1\beta H)_{28}$	0.400*	

[a] In mdyn/Å for stretches (κ) and mdyn Å/rad^2 for bends (H). The atoms joined by the bonds are given in parentheses, and the subscripts are the index numbers for the force constants. Asterisks indicate the force constants adjusted in the refinement; the remainder were fixed at the values taken from the NiOEP in-plane force field of ref 8.

The results of the calculation are given in Tables IV and V, where the calculated frequencies and isotope shifts are compared with the available experimental data. The assignments are based on NiOEP (see below) for which the corresponding frequencies are also listed. Table VI compares experimental frequencies between NiOEP and NiOEiBC (solid samples at low temperatures, in both cases) for the same modes classified according to parent (D_{4h}) symmetry and major local coordinate contributions. C–H stretching modes, which are not observed in the RR spectra, have been omitted. As in the case of NiOEP, modes mainly involving internal coordinates extending beyond the methylene carbon atoms are classified as ethyl modes and are listed separately in Table V, along with approximate mode descriptions. These descriptions are qualitative, and they are based on examination of the eigenvectors. Several of the ethyl modes mix extensively with the iBC skeletal modes, as evidenced by the isotope shifts (Table V). This is especially marked for the 1225-cm^{-1} ethyl twist, which is predicted to couple with $C_\alpha C_\beta$ stretching of the reduced

(22) Kratky, C.; Angst, C.; Johansen, J. E. *Angew. Chem., Int. Ed. Engl.* **1982**, *20*,. 211.
(23) Czernuszewicz, R. S.; Li, X. Y.; Spiro, T. G. *J. Am. Chem. Soc.* **1989**, *111*, 7024.
(24) Burgi, H.; Dunitz, J. D. *J. Am. Chem. Soc.* **1987**, *109*, 2924.
(25) Snyder, R. G.; Schachtschneider, J. H. *Spectrochim. Acta* **1965**, *21*, 169.

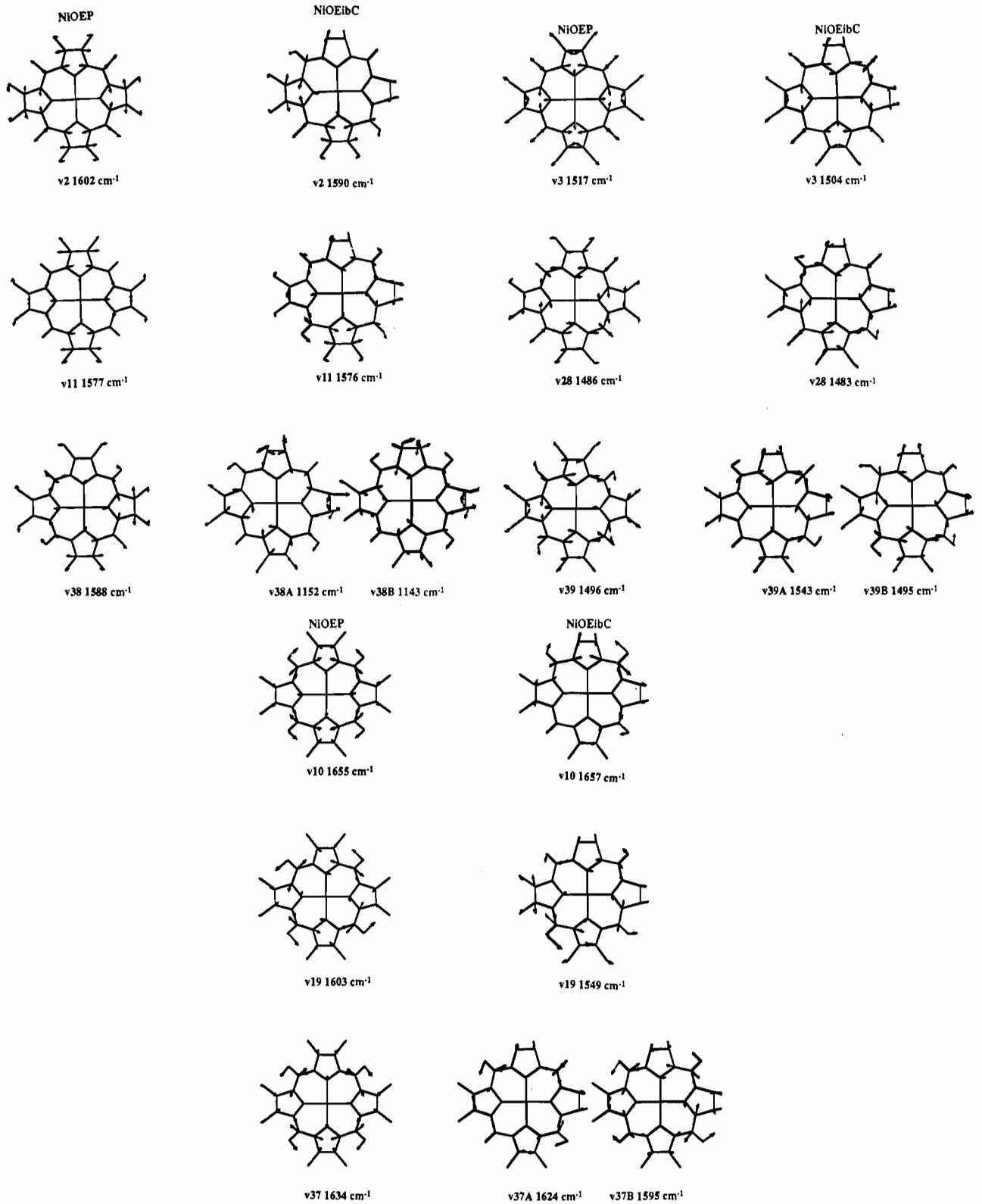

Figure 2. Eigenvectors for the 10 highest frequency skeletal modes of NiOEiBC, involving $C_\alpha C_m$ and $C_\beta C_\beta$ stretching, primarily, and comparisons with corresponding modes of NiOEP.

rings. The coupling is removed in the *meso*-d_3 isotopomer, raising the frequency back to that found for NiOEP, 1273 cm^{-1}. The four H atoms of the two pyrroline rings introduce 12 extra vibrational modes relative to NiOEP. Four of these are C–H stretches, and the remaining eight are mainly C–H bends. These coordinates are likewise assigned from examination of their eigenvectors and are labeled "pyrroline" in Table IV.

In Figure 2, calculated eigenvectors are compared for the 10 highest frequency skeletal modes among NiOEiBC and NiOEP. Two of these modes, ν_3 and ν_{11}, involve stretching of the pyrrole $C_\beta C_\beta$ double bonds, primarily; OEC and OEP have a third and a fourth $C_\beta C_\beta$ mode, ν_{38a} and ν_{38b}, which correlate with pyrroline $C_\beta C_\beta$ single-bond stretching modes of OEiBC at much lower frequency. The other eight modes, ν_{10}, ν_{37a}, ν_{37b}, ν_2, ν_{19}, ν_{39a}, ν_{39b}, and ν_{28}, involve stretching of the eight $C_\alpha C_m$ bonds in various phases. These modes involve significant motions of the *meso*-H atoms. For OEiBC, in contrast to OEP[8] and OEC,[7] some of the $C_\alpha C_m$ modes are substantially localized on the pyrrole (ν_{19}, ν_{28}) or pyrroline half of the macrocycle (ν_{10}, ν_{37a}, ν_{39a}). This is a consequence of energy factoring, the bonds being shorter and the

Table III. Off-Diagonal Force Constants for NiOEiBC

internal coord[a]	pyrroline ring	pyrrole rings
$(\kappa-\kappa)_{1,2}$		
1-1, 2-6, 4-6, 1-7, 6-8	0.430	0.430
1-4	0.470*[b]	0.430
2-3	0.230*	0.430
2-4	0.430*	0.230*
4-4	0.400*	0.370*
7-7	0.150	0.150
$(\kappa-\kappa)_{1,3}$		
1-2, 2-2	0.250	0.250
1-4, 4-7, 2-4, 2-6, 1-6	-0.250	-0.250
$(\kappa-H)_2$		
4-17, 1-11, 2-12, 2-16, 4-16, 2-18	0.245	0.245
2-13	0.160*	0.320
3-13	0.020*	0.320
3-19, 6-18, 6-19	0.320	0.320
1-12, 1-15, 1-14	0.100	0.100
4-22	0.120*	0.080*
6-23, 8-24	0.110	0.110
$(\kappa-H)_1$		
1-15, 1-12, 2-11, 6-12	-0.120	-0.120
1-12, 2-15, 4-12, 2-19, 6-13	-0.245	-0.245
1-22	0.080	0.080
$(H-H)_2$		
15-17	0.060	0.060
23-24	-0.070	-0.070

[a] *i-j*, interactions between diagonal force constants *i* and *j*, labeled according to the index numbers in Table II. $(H-H)_2$, bend-bend interaction between angles sharing two common atoms. $(\kappa-H)_1$, stretch-bend interaction between bond and angle sharing one common atom. $(\kappa-H)_2$, stretch-bend interaction between bond and angle sharing two common atoms. $(\kappa-\kappa)_{1,3}$, stretch-stretch interaction between two bonds separated by one atom. $(\kappa-\kappa)_{1,2}$, stretch-stretch interaction between two bonds sharing one atom. [b] Asterisks indicate the force constants were adjusted in the refinement, while the remainder were taken from the NiOEP force field of ref 8.

force constants being correspondingly higher on the pyrrole side. For the same reason, the frequencies do not segregate as cleanly into low and high values for symmetric and antisymmetric phasings of $C_\alpha C_m$ stretches, as they do in NiOEP. There is also significant mixing among modes of the same symmetry type at nearby frequencies (e.g. ν_{10} with ν_{37b}, ν_{28} with ν_{39a}). The OEiBC eigenvectors nevertheless show a significant memory of their parentage in the corresponding OEP modes in terms of the amplitudes and directions of the atomic motions.

Modes above 1480 cm^{-1}, involving $C_\alpha C_m$ and pyrrole $C_\beta C_\beta$ stretching, are more sensitive to ^{15}N substitution in OEiBC then in OEP. This effect is accommodated in the calculations by increasing slightly (0.04 mdyn/Å) the coupling constant between $C_\alpha C_m$ and NC_α stretching ($(\kappa-\kappa)_{1,2}$ values marked with an asterisk in Table III). This increased coupling might reflect the smaller π-conjugation pathway in OEiBC due to the reduction of two $C_\beta C_\beta$ bonds.

Four of the calculated *meso-d_3* shifts deviate significantly from the observed shifts, indicating that the associated eigenvectors are incorrect. The calculated shifts are 15–21 cm^{-1} for ν_{37}, ν_{39}, ν_{39a}, and ν_{39b}, whereas the observed shifts are 1–3 cm^{-1}. For ν_{19} on the other hand, the calculated shift, 4 cm^{-1}, is much smaller than the observed shift, 18 cm^{-1}. These discrepancies would be remedied if the calculated *meso*-hydrogenic motions were concentrated on the unsubstituted position γ for ν_{37a}, ν_{39a}, and ν_{39b}, but on the three substituted positions, α, β, and δ, for ν_{19}. These motions are strongly affected by changes in the $C_\alpha C_m/C_\alpha C_m$ stretch–strech interaction force constants. In the absence of additional isotopic data, however, further refinement of the force field is arbitrary. The required changes in the hydrogenic motions are unlikely to alter the pattern of the C–C and C–N bond stretches materially.

2. Assignments. Figure 3a–c compares RR spectra with 406.7 nm excitation for NiOEiBC and its *meso-d_3* and ^{15}N isotopomers. The spectra were obtained on solid samples at 10 K to sharpen the bands and improve the signal. Parallel and perpendicular scattering components were measured separately for the natural-abundance and *meso-d_3* samples in order to assess the band polarizations. Although multiple scattering in polycrystalline samples tends to scramble the polarization, this effect is suppressed when the sample is highly absorbing, and reasonable approxi-

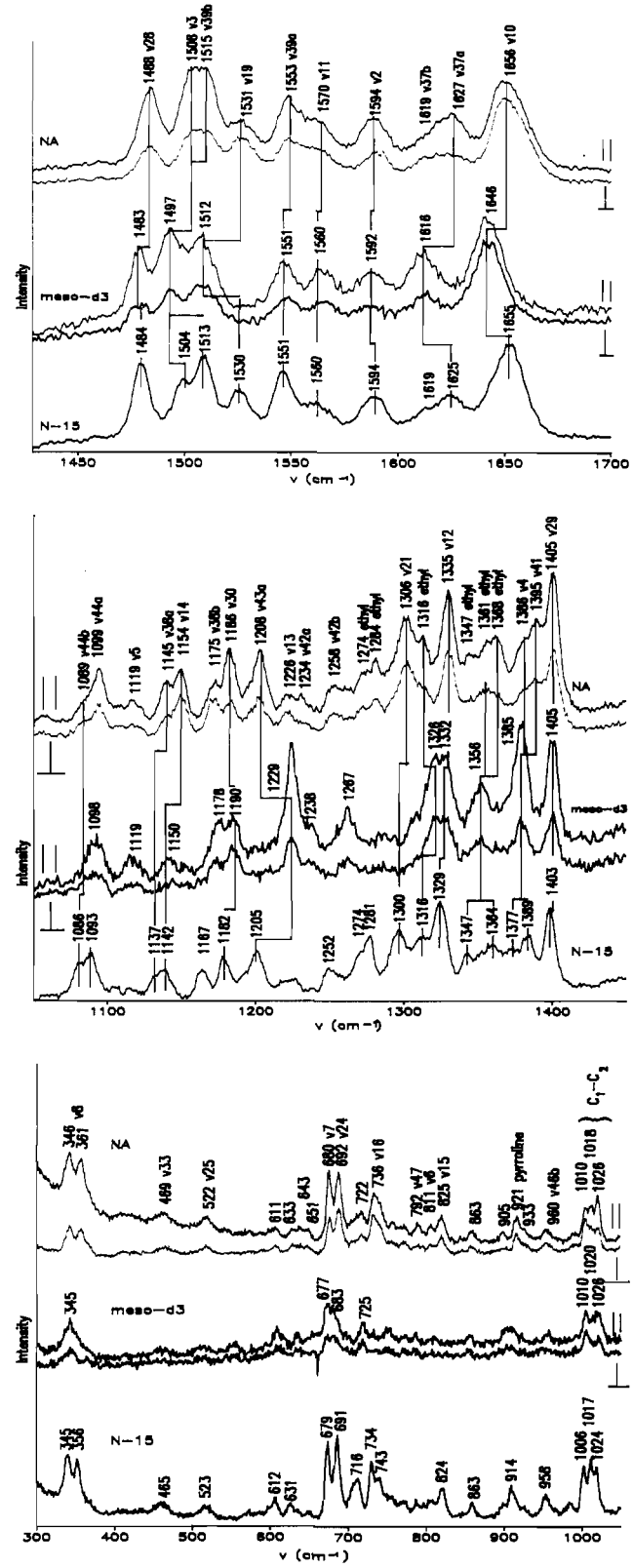

Figure 3. (a) Top: Comparison of 406.7-nm-excited RR spectra in the 1400–1700-cm^{-1} region of NiOEiBC (KBr pellet, 10 K) in parallel and perpendicular polarization for the natural-abundance (NA), *meso-d_3*, and ^{15}N isotopomers. The band frequencies (cm^{-1}) are marked and NiOEP-derived assignments are indicated. Conditions: slit width, 6 cm^{-1}; step size, 1 cm^{-1}, collection time, 3 s/step. (b) Middle: Comparison as in part a, but 1050–1450 cm^{-1}. (c) Bottom: Comparison as in part a, but 300–1050 cm^{-1}.

Table IV. Calculated and Observed Vibrational Frequencies and Isotope Shifts for NiOEiBC (cm^{-1}) in Comparison to NIOEP

calcd				obsd			obsd NiOEP[d]		
ν,[a] cm^{-1}	$\Delta(d_3)$[b]	$\Delta(^{15}N)$[b]	assgnt[c]	ν,[a] cm^{-1}	$\Delta(d_3)$	$\Delta(^{15}N)$	ν, cm^{-1}	$\Delta(d_4)$	$\Delta(^{15}N)$
1657 B	12	0	ν_{10}	1656 ap	10	1	1655	10	0
1624 A	20	0	ν_{37a}	1627 p	11	2	(1637)	(17)	(0)
1590 A	3	0	ν_2	1594 p	3	1	1602	1	1
1595 B	15	1	ν_{37b}	1619	···	1	(1637)	(17)	(0)
1576 B	4	1	ν_{11}	1568 dp	1	2	1577	1	1
1549 B	4	1	ν_{19}	1531 ap	···	1	1603	22	1
1543 A	21	2	ν_{39a}	1553 p	2	2	1501	7	0
1504 A	10	2	ν_3	1508 p	11	4	1520	8	1
1495 B	12	3	ν_{39B}	1515	3	2	1501	7	0
1483 A	6	4	ν_{28}	1488 p	4	4	1483	5	3
1447 A	1	1	ν_{40}				1396	4	0
1443 B	1	1	ν_{40}				1396	4	0
1410 B	2	1	ν_{20}				1393	0	0
1409 A	3	2	ν_{29}	1405 p	0	2	1407	2	1
1402 B	2	1	ν_{41}				(1346)	(4)	(5)
1402 A	2	1	ν_{41}	1394 p	9	5	(1346)	(4)	(5)
1381 A	2	2	ν_4	1386 p	1	9	1381	1	7
1342 B	1	4	ν_{12}	1335 ap	3	6	(1330)	(12)	(6)
1315 B	408	3	ν_{21}	1306 dp	···	6	1307	420	4
1260 B	13	2	ν_{42}	1258 p	···	6	1231	283	3
1247 A	375	3	ν_{42}	1235	···	···	1231	283	3
1239 B	385	4	ν_{13}	1226 ap	···	···	1220	272	2
1219 A	+23	7	ν_{43}	1208 p	+21	3	1153	+32	8
1195 B	+29	8	ν_{43}				1153	+32	8
1156 A	6	2	ν_{30}	1186 p	+4	4	1159	0	10
1152 A	+4	4	ν_{38a}	1145 p	+5	12	1604	0	0
1143 B	+24	2	ν_{38b}	1175 dp	+3	1	1604	0	0
1124 A	1	8	ν_5	1119 p	0	0	1138	0	7
1124 B	+17	9	ν_{14}	1154 ap	···	12	1131	+55	12
1115 A	+84	8	ν_{44}				1133	+18	12
1115 B	2	8	ν_{44}				1133	+18	12
1100 B	+139	4	ν_{22}				1121	+81	0
1047 A	+5	1	ν_{45}	994	+1	0	996	0	5
1047 B	2	2	ν_{45}				996	0	5
1037 A	28	12	ν_{31}				1015	12	9
1026 B	15	1	ν_{23}	1060 ap	0	0	1058	0	0
1000 B	+58	7	pyrroline						
999 A	+34	9	pyrroline						
958 A	4	12	ν_{32}	905 p			938	4	0
955 B	2	9	pyrroline						
924 B	+3	1	ν_{46}	921 dp	···	0	927	8	3
925 A	3	0	ν_{46}	960 dp	0	2	927	8	3
917 A	+8	3	pyrroline						
882 B	4	4	pyrroline						
861 A	5	0	pyrroline	863	···	···			
806 A	3	6	ν_6	811	···	···	804	3	5
768 A	3	1	ν_{47}	792	···	···	(791)	(0)	(5)
762 B	6	2	ν_{47}				(791)	(0)	(5)
744 B	118	1	ν_{15}	825 dp	···	1	751	68	3
721 B	+22	0	pyrroline						
691 A	43	0	ν_{48}				605	5	0
690 B	+15	2	ν_{16}	737 ap	···	1	740	+12	0
683 B	5	1	ν_{48}				605	5	0
679 A	1	0	ν_7	680	4	1	674	6	3
612 B	9	3	ν_{24}	692	10	2	597	15	1
546 B	0	1	ν_{25}	521 dp	0	0	551	6	0
528 A	1	0	ν_{49}				544	1	0
518 B	3	1	ν_{49}				544	1	0
480 A	1	2	ν_{33}	469 p	0	2	493	3	1
405 A	1	1	ν_{50}				(358)	(1)	(1)
403 B	2	1	ν_{50}				(358)	(1)	(1)
391 A	1	0	ν_8	346 p/361 p[e]	0/−	0/5	360/343[e]	7/0	2/1
350 A	4	1	pyrroline						
335 A	0	0	ν_{51}				328	6	0
333 B	1	0	ν_{51}				328	6	0
270 B	0	0	ν_{17}				305	0	0
265 A	0	0	ν_9	299/281[e]			263/274[e]	1/0	2/1
208 B	0	1	ν_{26}	244			(243)	(0)	(0)
202 B	0	0	ν_{52}				263	3	2
201 A	0	0	ν_{52}				263	3	2
200 A	0	0	ν_{34}	202			197	0	0
197 B	0	0	ν_{18}				168	0	0
158 A	0	0	ν_{35}				144	3	0
130 B	0	0	ν_{53}				212	0	0
117 A	0	0	ν_{53}				212	0	0

[a] Symmetries (A, B) are listed for the calculated bands, and polarizations (p, polarized; dp, depolarized; ap, anomalously polarized) are listed for the RR bands at the indicated frequencies. [b] Frequency downshifts (+upshift) upon *meso*-d_3 and ^{15}N substitution. [c] Based on eigenvector comparisons with NiOEP.[8] Pyrroline refers to the new vibrational modes introduced upon ring reduction. [d] Values in parentheses are calculated. Fron ref 8. [e] Doublets attributed to ethyl rotational isomers.[8]

Table V. *Vibrational* Frequencies and Isotope Shifts for NiOEiBC Ethyl Modes

calcd				obsd		
ν, cm^{-1}	$\Delta(d_3)$	$\Delta(^{15}N)$	assgnt[a]	ν, cm^{-1}	$\Delta(d_3)$	$\Delta(^{15}N)$
1475	0	0	et scissors			
1474	0	0	et scissors			
1474	0	0	et scissors			
1474	0	0	et scissors			
1472	0	0	et scissors			
1472	2	0	et scissors			
1471	2	0	et scissors			
1468	0	0	et scissors			
1367 B	2	1	et wag			
1364 A	0	1	et wag	1368 p	12	4
1361 B	0	1	et wag			
1358 A	0	0	et wag	1361 p	5	0
1358 B	0	0	et wag			
1354 A	0	2	et wag			
1351 B	0	0	et wag	1347	0	0
1350 A	0	0	et wag			
1303 A	+7	4	et twist	1316	+10	0
1293 A	+3	3	et twist			
1291 B	0	5	et twist	1284 ap	...	3
1288 B	0	3	et twist			
1287 A	0	5	et twist	1276	...	2
1283 B	0	3	et twist			
1275 A	0	1	et twist			
1252 B	+21	4	et twist			
1024 A	0	1	c1–c2	1066	1	2
1022 B	0	1	c1–c2			
1018 A	0	1	c1–c2	1018 p	+2	1
1015 A	0	0	c1–c2			
1015 B	0	0	c1–c2			
1005 B	2	1	c1–c2	1010 ap	0	2
1001 B	0	0	c1–c2			
1001 A	0	1	c1–c2			
816 B	6	1	β12			
780 B	0	4	et rock			
756 A	4	2	et rock			
754 B	3	2	et rock			
745 A	0	1	et rock			
721 B	7	1	et rock			
721 A	7	0	et rock			
710 A	11	1	β12			
704 A	1	1	β12			
672 B	1	1	et rock			
589 A	0	1	et rock			
552 A	2	1	β12			
470 B	2	2	β12			
455 A	1	1	β12			
453 B	0	0	β12			
387 B	0	0	β12			
304 A	1	1	$\gamma\beta$1			
301 A	1	1	$\gamma\beta$1			
290 B	0	0	$\gamma\beta$1			
247 A	1	0	$\gamma\beta$1			

[a] From ref 8.

mations to the isotropic sample polarizations are then obtained.[26] It is easy to tell that some bands, e.g. ν_{10} (1656 cm^{-1}), are depolarized or anomalously polarized, while others, e.g. ν_2 (1594 cm^{-1}), are polarized. For still others, especially weak bands, the polarization is uncertain. Figure 4 shows infrared spectra of NiOEiBC and NiOEiBC-d_3.

The RR polarizations, together with the isotope shifts and the frequency correspondences with NiOEP, were used to assign the observed bands to the calculated modes. The RR and infrared spectra contain many more bands than those of NiOEP because of the lowered symmetry of NiOEiBC, C_2. The infrared modes, E_u in D_{4h} symmetry, become Raman-active, and they split into A and B symmetry modes. These modes retain strong intensity in the IR spectra, which additionally show Raman modes, activated by symmetry lowering. The mode correlation from D_{4h}

(26) Strommen, D. P.; Nakamoto, K. In *Laboratory Raman Spectroscopy*; John Wiley: 1984; p 88.

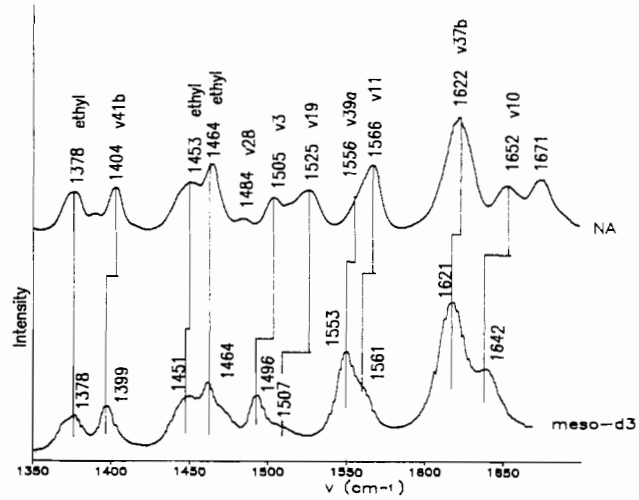

Figure 4. FTIR spectra (KBr pellet) of NiOEiBC and its *meso*-d_3 isotopomer.

symmetry are as follows: A_{1g}, $B_{2g} \rightarrow A$; A_{2g}, $B_{1g} \rightarrow B$. The RR bands are polarized for A modes and depolarized or anomalously polarized for B modes. As have been noted elsewhere,[15] the chlorin and iBC C_2 axes are rotated by 45° with respect to each other, so that the B_{1g} and B_{2g} correlations are switched. B_{2g}-derived modes are depolarized or anomalously polarized for chlorin but polarized for iBC's and vice versa for B_{1g} modes. A clear demonstration of the retention of mode character is provided by the highest frequency RR band, which is near 1650 cm^{-1} in all three Ni macrocycles. The band is depolarized for NiOEP, polarized for NiOEC, and anomalously polarized for NiOEiBC, showing it to be the B_{1g}-derived mode ν_{10} in each case.

The 10 highest frequency skeletal modes whose eigenvectors are diagrammed in Figure 2 are readily assigned to the ten bands observed between 1480 and 1660 cm^{-1}. The polarizations and isotope shifts leave little doubt about the mode correlations. In the complex mid-frequency region, however, assignments are more tentative. Near 1400 cm^{-1}, the Soret-excited spectrum of NiOEP is dominated by the strong ν_4 band at 1383 cm^{-1}. This mode is the pyrrole half-ring stretch,[8] which shifts down 7 cm^{-1} on ^{15}N substitution, but is insensitive to meso deuteration. The NiOEiBC spectrum is quite different. It has a strong band at 1405 cm^{-1}, which, however, shifts only 2 cm^{-1} on ^{15}N substitution, while the next band, at 1395 cm^{-1}, shows a 10-cm^{-1} d_3 shift. The third band in this region, at 1386 cm^{-1}, corresponds in frequency and isotope shift pattern (1 cm^{-1} d_3, 9 cm^{-1} ^{15}N) to ν_4, but is quite weak. We surmise that the symmetry lowering in NiOEiBC allows a shift in RR intensity from ν_4 to nearby newly symmetric modes, which we assign to ν_{40a} and ν_{29}; all three bands are polarized. Other prominent mid-frequency bands whose assignments are secured by polarizations and isotope shifts are $\nu_{12}(B_{1g})$, another half-ring stretch, ν_{21} (A_{2g}, 1306 cm^{-1}), the C_m–H rotational mode, and ν_{43a} (E_u, 1208 cm^{-1}), an asymmetric half-ring stretch, which shifts up 21 cm^{-1} on d_3 substitution because of uncoupling with the 1253-cm^{-1} ν_{42a} C_m–H bending mode. Three bands are seen near 1024 cm^{-1}, where NiOEP has a prominent RR band that was assigned to stretching of the ethyl C_1–C_2 bonds on the basis of its sensitivity to deuteration of the methylene groups. Its enhancement was attributed to an ethyl–porphyrin hyperconjugative interaction.[8] The three NiOEiBC bands, at 1010, 1016, and 1024 cm^{-1} are probably C_1–C_2 stretching in character as well. The 1010-cm^{-1} band is anomalously polarized and must be a B-symmetry combination of the C_1–C_2 stretches. There are weak candidate bands for CH_2 twisting and wagging modes, which have also been identified in the NiOEP spectra. The low frequency region of the RR spectra, shown in Figure 3c, is not as rich, but several bands are seen and suggested assignments are given. The strong ν_7 band at 680 cm^{-1} is reminiscent of NiOEP as is the strong doublet at 346/361 cm^{-1}. This doublet has been atttributed to conformational isomers of the ethyl groups in NiOEP,[8] and the same explanation probably holds for NiOEiBC.

Table VI. Comparison of Experimental NiOEP[a] and NiOEiBC[b] Skeletal Mode Frequencies

	A_{1g} (A)		B_{1g} (B)		A_{2g} (B)		B_{2g} (A)		E_u (A,B)	
sym → coord	ν_i	ν, cm^{-1}	ν_i	ν, cm^{-1}	ν_i	ν, cm^{-1}	ν_i	ν, cm^{-1}	ν_i	ν, cm^{-1}
$\nu(C\alpha Cm)_{asym}$			ν_{10}	1655	ν_{19}	1603			ν_{37}	1637
				1656 ap		**1531 ap**				**1627 p, 1619 dp**
$\nu(C\beta C\beta)$	ν_2	1602	ν_{11}	1577					ν_{38}	1604
		1594 p		**1568 dp**						**1145 p, 1175 dp**
$\nu(C\alpha C_m)_{sym}$	ν_3	1520					ν_{28}	1483	ν_{39}	1501
		1508 p						**1488 p**		**1553 p, 1515**
ν(pyr $^1/_4$ ring)					ν_{20}	1393	ν_{29}	1407	ν_{40}	1396
								1405 p		
ν(pyr $^1/_2$ ring)$_{sym}$	ν_4	1381	ν_{12}	1330					ν_{41}	1346
		1386 p		**1335 ap**						**1394 p**
$\delta(C\mu H)$			ν_{13}	1220	ν_{21}	1307			ν_{42}	1231
				1226 ap		**1306 dp**				**1258 p, 1235**
$\nu(C\beta C1)_{sym}$	ν_5	1138	ν_{14}	1131					ν_{44}	1153
		1119 p		**1154 ap**						
ν(pyr $^1/_2$ ring)$_{asym}$					ν_{22}	1121	ν_{30}	1159	ν_{43}	1133
								1186 p		**1208 p**
$\nu(C\beta C1)_{asym}$					ν_{23}	1058	ν_{31}	1015	ν_{45}	996
						1060 ap				**994**
δ(pyr def)$_{asym}$					ν_{24}	597	ν_{32}	938	ν_{46}	927
						692		**905 p**		**930, 921 dp**
ν(pyr breath)	ν_6	804	ν_{15}	751					ν_{47}	766
		811		**825 dp**						
ν(pyr def)$_{sym}$	ν_7	674	ν_{16}	746					ν_{48}	605
		680 p		**737 ap**						
ν(pyr rot)					ν_{25}	551	ν_{33}	493	ν_{49}	544
						521 dp		**469 p**		
ν(NiN)	ν_8	343/360	ν_{18}	168					ν_{50}	358
		346 p/361 p								
$\delta(C\beta C1)_{asym}$					ν_{26}	243	ν_{34}	197	ν_{51}	328
						244		**202**		
$\delta(C\beta C1)_{sym}$	ν_9	274/263	ν_{17}	305					ν_{52}	263
δ(pyr trans)		**299/281**					ν_{35}	144	ν_{53}	212

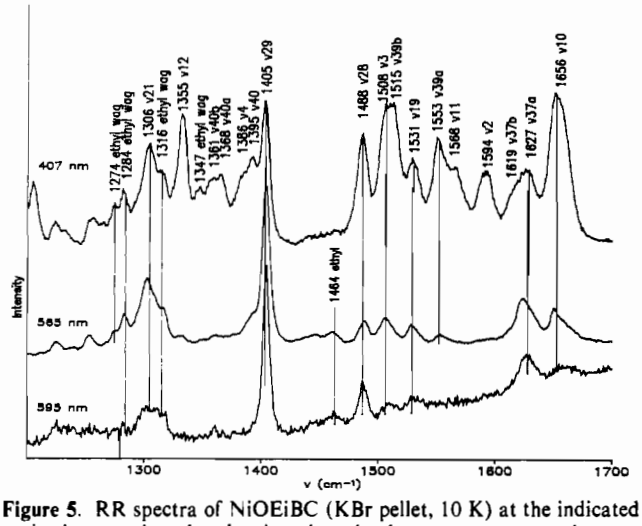

Figure 5. RR spectra of NiOEiBC (KBr pellet, 10 K) at the indicated excitation wavelengths, showing altered enhancement patterns in resonance with the B and Q bands.

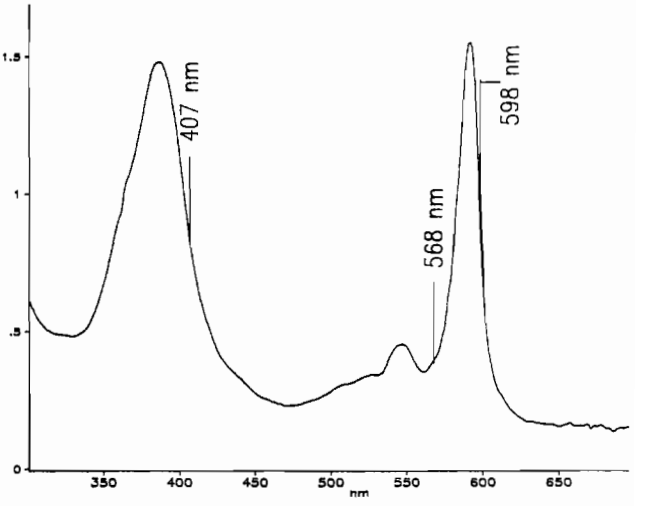

Figure 6. NiOEiBC absorption spectrum in benzene, showing the B and Q bands, and the laser excitation wavelengths for the spectra in Figure 5.

3. Enhancement Mechanisms. Figure 5 shows how the RR enhancement pattern varies for three excitation wavelengths, 406.7, 568.2, and 598.0 nm, whose relationship to the NiOEiBC absorption bands is shown in Figure 7. The two main bands, 380 and 590 nm, are the B and Q bands while the weak 550-nm band is the Q_1 vibronic sideband on Q. The iBC visible electronic transitions can be understood on the basis of Gouterman's four-orbital model[27] for porphyrin, diagrammed in Figure 8. The two absorption bands are due to transitions from the two highest filled orbitals, a_{1u} and a_{2u}, to the degenerate pair of lowest unoccupied orbitals, e_g*. The symmetry labels are for a D_{4h} porphyrin, but they work for iBC as well, because the axes formed by the (pyrrole)N–Ni–N(pyrroline) bonds remain equivalent even if they are no longer symmetry axes. Consequently, the two e_g* orbitals remain degenerate. In porphyrin absorption spectra, the Q band is much weaker than the B bands due to configuration interaction between the orbital excitations from a_{1u} and a_{2u}.[27] The excitations are fully mixed, and the Q_0 band intensity vanishes, when a_{1u} and a_{2u} are accidentally degenerate; the Q_1 band, however, retains about 10% of the B band intensity through Q/B vibronic coupling. The reduction of two pyrrole rings in iBC selectively raises the energy of the a_{1u} orbital, since it is concentrated on the pyrrole C_α and C_β atoms, while the a_{2u} orbital is concentrated of the C_m and N atoms. Consequently, configuration interaction is diminished and the Q_0 band is much stronger than in porphyrins. Indeed, it is nearly as strong as the B band (the B band is broader and therefore retains a larger integrated intensity).

In porphyrin RR spectroscopy, excitation in the region of the B band enhances mainly totally symmetric mode via the dominant

(27) Gouterman, M. J. *Mol. Spectrosc.* **1961**, *6*, 138.

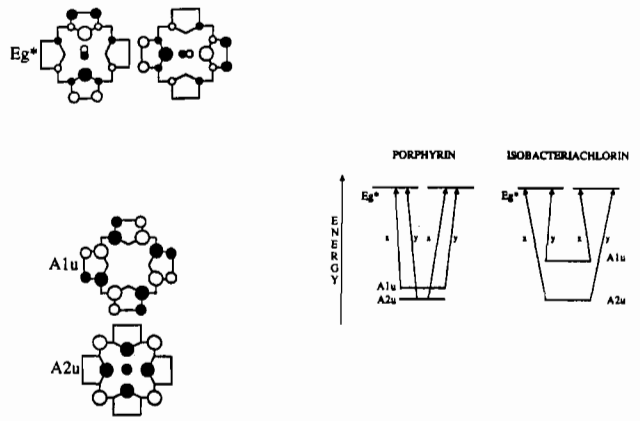

Figure 7. Frontier molecular orbitals of porphyrin derived from the four orbital model and correlation diagram indicating the effect of ring reduction from porphyrin to iBC on orbital energy levels.

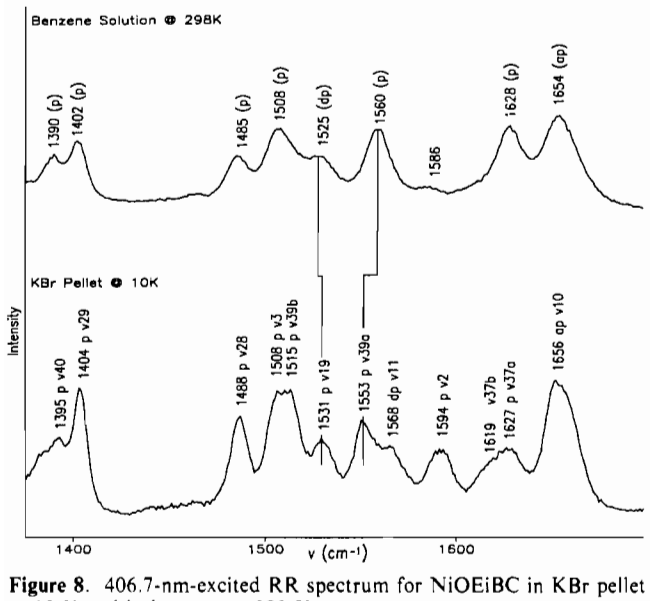

Figure 8. 406.7-nm-excited RR spectrum for NiOEiBC in KBr pellet at 10 K and in benzene at 298 K.

Franck–Condon (A term) scattering mechanism while excitation in the region of the Q bands enhances mainly non totally symmetric modes via the vibronic (B term) mechanism, since the low transition moment suppresses the A term.[1] For iBC, however, the A term should also dominate Q-resonant spectra. Indeed, the 595 nm-excited spectrum (Figure 5) does contain bands that arise mostly (but not exclusively) from A symmetry modes. The most striking aspect of the spectrum, however, is that it is dominated by a single band, ν_{29} which is several times stronger than the others. Evidently, the origin shift of the Q_0 transition is concentrated along the ν_{29} coordinate. In contrast, several symmetric modes have intensity comparable to ν_{29} in the B-resonant spectrum excited at 406.7 nm, ν_2, ν_3, ν_{37a}, ν_{39a}, and ν_{28}. We attribute this difference to the differing a_{1u} and a_{2u} orbital patterns mentioned above, since the energy increase of the a_{1u} orbital, and the consequent loss of configuration interaction, means that the B and Q electronic transitions are primarily due to the individual $a_{2u} \rightarrow e_g^*$ and $a_{1u} \rightarrow e_g^*$ excitations, respectively. The orbital patterns, illustrated in Figure 7, show that the pyrrole $C_\alpha C_\beta$ interaction is bonding for the a_{1u} orbital but antibonding for the e_g^* orbital and that the main consequence of the $a_{1u} \rightarrow e_g^*$ excitation should be a lengthening of the $C_\alpha C_\beta$ bonds. These bonds are importantly involved in ν_{29}, a pyrrole quarter ring stretch,[8] and the dominance of this mode in the Q-band-resonant RR spectrum can be understood on this basis. On the other hand, the concentration of the a_{2u} orbital on the C_m atoms may explain the enhancement of several high-frequency A-symmetry modes in the B-band-resonant spectrum, since they all have substantial contributions from $C_\alpha C_m$ stretching.

Excitation of 568.2 nm, between the Q_0 and Q_1 bands, was expected to emphasize vibronic scattering.[1] Indeed, B-symmetry modes do show a gain in relative enhancement compared to 598.0-nm excitation, even though the ν_{29} band is still dominant. The B-symmetry augmentation is seen most clearly in the intensities of ν_{11} and ν_{19} in relation to the nearby ν_{28} and in the apparent frequency shift of the ν_{37a}/ν_{37b} envelope as ν_{37b} gains in relative intensity with 568.2-nm excitation.

Another interesting aspect of the iBC enhancement pattern is the pronounced enhancement of B-symmetry modes with excitation in the B absorption band. The strongest band in the 406.7-nm-excited RR spectrum is ν_{10}. Several other B-symmetry modes, e.g. ν_{39b}, ν_{12}, and ν_{21}, are comparable to the strongest A-symmetry modes. This strong vibronic activity can be related to the Jahn–Teller effect, which is believed to account for the appearance of B_{1g} and B_{2g} modes in B-band-resonant RR spectra of metalloporphyrins. The Jahn–Teller effect is suppressed, however, by the same configuration interaction between the $a_{1u} \rightarrow e_g^*$ and $a_{2u} \rightarrow e_g^*$ orbital excitations that suppress the transition moment of the porphyrin Q band. Shelnutt et al.[28] showed that B_{1g} and B_{2g} mode intensity in the B-band-resonant RR spectra correlates with the absorption strength of the Q_0 band. Both effects are related to the a_{1u}–a_{2u} energy separation. As noted above, the e_g^* component orbitals remain degenerate in iBC even though they are transformed into A- and B-symmetry orbitals. The vibronic coupling between them is the same mechanism as the Jahn–Teller effect. Because of the large a_{1u}–a_{2u} energy separation, there is little configuration interaction, as evidenced by the strong iBC Q band, and Jahn–Teller activity is therefore not suppressed. The result is that vibronic and Franck–Condon scattering mechanisms have comparable strengths in the B-band-resonant RR spectrum. The Jahn–Teller activity can also account for the large width of the B band in the NiOEiBC absorption spectrum (Figure 6). The Q band is narrower and the relative enhancement of B-symmetry modes is low in the Q excited RR spectrum (Figure 5). Thus, Jahn–Teller activity is evidently lower in the Q than in the B state. We infer that the $a_{1u} \rightarrow e_g^*$ orbital excitations are less susceptible to vibronic mixing than are the $a_{2u} \rightarrow e_g^*$ excitations.

Figure 8 reveals significant differences between the RR spectra of NiOEiBC in a solid sample at low temperature and in solution at room temperature. The solid spectrum at room temperature (not shown), although somewhat noisy, was essentially the same as that at low temperature, so the differences in Figure 8 are attributable to the compound being in solution versus in the solid state. In solution, the bands associated with ν_{37a} and ν_{39a} become appreciably stronger while the bands associated with ν_{37b}, ν_2, and ν_{39b} become weaker. Two bands shift in frequency: ν_{39a} shifts up by 7 cm^{-1} while ν_{19} shifts down by 6 cm^{-1} in solution. These differences may reflect subtle changes in the macrocycle conformation between solid and solution. For NiOEP, substantial frequency downshifts are seen for several high-frequency modes between ruffled and planar crystalline polymorphs.[23] In solution, the frequencies adopt intermediate values, reflecting a less markedly ruffled structure. This is not the pattern observed for NiOEiBC, which probably retains its ruffled structure in solution. Since the OEiBC core size is expanded relative to that of OEP, the ruffling tendency is stronger and less susceptibile to relaxation when packing constraints are removed. The alteration giving rise to the intensity changes and slight frequency shifts is uncertain.

4. Core-Size Dependence. Metalloporphyrin skeletal frequencies in the 1450–1650-cm^{-1} region correlate negatively with the porphyrin core size,[29,30] mainly because the stretching of the C_aC_m bonds, the main locus of the core expansion stress, is a significant contributor to these modes.[8] The core size dependence accounts for the sensitivity of these frequencies to the ligation and spin state of iron porphyrin complexes, since the core expands for

(28) Shelnutt, J. A.; Cheung, L. D.; Cheng, C. C.; Yu, N. T.; Felton, R. H. *J. Chem. Phys.* **1977**, *66*, 3387.
(29) Parthasarathi, N.; Hansen, C.; Yamaguchi, S.; Spiro, T. G. *J. Am. Chem. Soc.* **1987**, *109*, 3865.
(30) Choi, S.; Spiro, T. G.; Langry, K. C.; Smith, K. M.; Budd, L. D.; LaMar, G. N. *J. Am. Chem. Soc.* **1982**, *104*, 4345.

Table VII. List of RR Frequencies (cm^{-1}) with Polarization for OEiBC Complexes

$Fe^{III}DMSO_2$[a]	Fe^{II}(1,2-DiMeIm)[b]	Fe^{II}_2O[c]	Fe^{II}(*N*-MeIm)$_2$[b]	Fe^{III}(*N*-MeIm)$_2$[a]	Fe(II)[b]	Ni(II)[b]	assgnt
1619 ap	1616 ap	1637 ap	1639 ap	1640 ap	1635 ap	1654 ap	ν_{10}
1590 p	1590 p	1607 p	1615 p	1600 p	1617 p	1629 p	ν_{37a}
		1600	1601 p		1609 p		ν_{37b}
1561 p	1544 p	1547	1580 p	1575 p	1589 p	1586	ν_2
			1563 p				
			1545 p	1548 p	1547 p	1558 p	ν_{39a}
	1507 ap[d]	1517 ap	1525 ap	1511 dp[e]	1513 dp	1527 dp	ν_{19}
1479 p	1486 p	1502 p	1495 p	1505 p		1515 p[f]	ν_{39b}
1469 p	1472 p	1485 p	1486 p	1490 p	1487 p	1507 p	ν_3
1458 p	1461 p	1472 p	1469 p	1473 p	1474 p	1487 p	ν_{28}
	1450 p	1459 p			1462 p		ν_{40a}
1422 p					1451 p		ν_{40b}
1393 p	1391 p[d]	1397 p		1394 dp	1396 p	1402 p	ν_{29}
	1383 p	1384 p	1388 p	1380 p	1385 p	1390 p	ν_{41a}
1374 p	1367 p	1372 p	1365 p	1366 p		1386 p[f]	ν_4

[a] DMSO solution. [b] Benzene solution. [c] From ref 15. [d] From Q-band excitated spectra (568 nm). [e] Shoulder. [f] Seen in KBr pellet at low temperature.

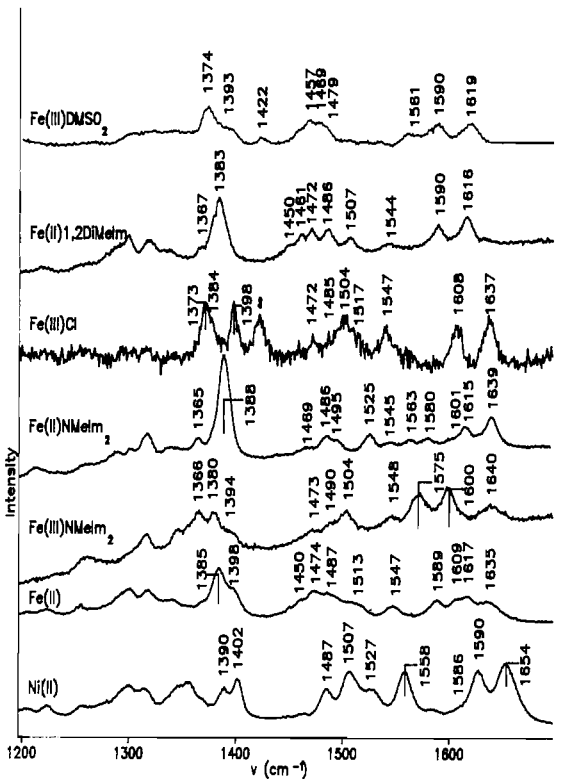

Figure 9. 406.7-nm-excited RR spectra of the indicated OEiBC complexes. The solvent was DMSO for the $Fe^{II}(DMSO)_2$, and Fe^{III}(1,2-DiMeIm)$_2$ complexes, CH_2Cl_2 for the $Fe^{III}Cl$ complex, and benzene for the others. Solvent peaks are double-starred.

high-spin complexes, relative to low- or intermediate-spin complexes, and it contracts to an intermediate value when the iron atom is displaced from the porphyrin plane in a five-coordinate high-spin complex. Similar core-size correlations are seen for the corresponding frequencies of metallochlorins,[31] although the slopes are different.

RR spectra are shown in Figure 9 for iron–OEiBC complexes of the same composition used previously to construct core-size plots for porphyrins and chlorins, while Figure 10 shows the core-size plot for the OEiBC complexes. The frequencies used in constructing this plot are listed in Table VII. The core sizes are not those of the iBC complexes themselves for which structural data are unavailable, but rather the standard set of porphyrin core-sizes used in both the porphyrin[29] and chlorin[31] core-size plots. A general trend can readily be discerned, and reasonably straight

(31) Ozaki, Y.; Iriyama, K.; Ogoshi, H.; Kitagawa, T. *J. Phys. Chem.* **1986**, *90*, 6105.

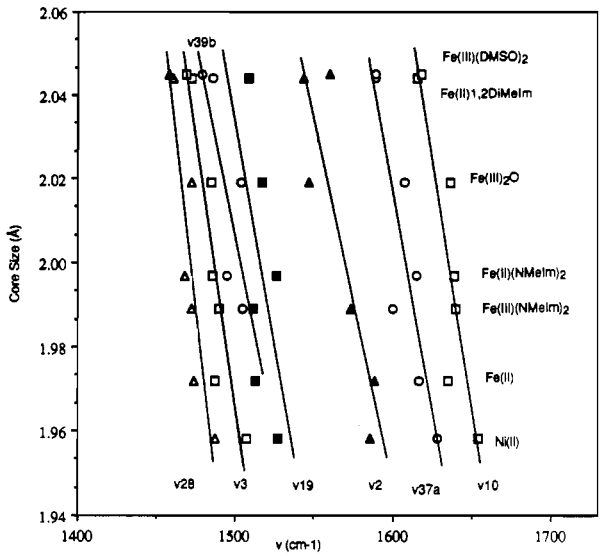

Figure 10. Plot of OEiBC RR frequencies (cm^{-1}) for the indicated complexes against the core size of the corresponding porphyrin complex (see ref 29 for a list of the reference structures).

Table VIII. Slopes and Intercepts of the Core-Size Correlations[a]

	K			*A*		
mode	OEP[b]	OEC[b]	OEiBC[c]	OEP[b]	OEC[b]	OEiBC[c]
ν_{10}	494.9	471.9	431.0	5.30	5.46	5.80
ν_3	413.8	346.8	401.6	5.63	6.33	5.70
ν_2	322.3	404.3	588.5	6.93	5.94	4.61
ν_{19}	576.3	331.8	480.7	4.74	6.76	5.15[d]
ν_{37a}			483.8			5.32
ν_{28}			308.0			6.78
ν_{39b}			545.2			4.76

[a] ν (cm^{-1}) = $A - Kd$ (Å). [b] Reference 4. [c] This work. [d] Weak correlation, R = 0.26 vs >0.6 for the other bands.

lines can be drawn through the data. The slopes, however, deviate significantly from those of the corresponding porphyrin or chlorin modes, as seen in Table VIII. . For ν_{10}, there is a progressive decrease in core-size sensitivity from OEP to OEC to OEiBC while for ν_2 there is a progressive increase. The sequence is irregular for ν_3 and ν_{19}; OEC and OEiBC both show lower sensitivity but more so for OEC. The variability of the slopes is connected to some extent with the redistribution of the C_aC_m stretching contribution to the eigenvectors (Figure 2). It must also be influenced by the real structural differences among the macrocycles: (1) The reduction of a pyrrole ring to pyrroline expands the natural radius of the macrocycle slightly. Consequently, the stress at the methine bridges should be smaller for a given increase in the metal ion radius. (2) Pyrroline reduction also increases the flexibility of the macrocycle toward out-of-plane distortions. A nice demon-

stration of this trend is the increase in the ruffling distortion seen for the Ni(II) complexes of tetramethylporphyrin, -chlorin, and -isobacteriochlorin.[16] The ruffling accommodates metal–N distances that are smaller than the natural macrocycle radius. They can also serve to dampen the stresses associated with variations in the metal ion size.

Deviations from the core-size plots are seen for the bis(imidazole) and mono(2-methylimidazole) adducts of iron(II) porphyrins,[29,30] models for reduced cytochromes-*b* and for deoxymyoglobin, respectively. For the bis(imidazole) complex, the deviations are attributed to the effects of Fe $d_\pi \rightarrow$ porphyrin π^* back-donation and have been explained qualitatively in terms of the e_g^* orbital pattern. For the 2-methylimidazole adduct, the reason for the deviations is less clear. Back-donation should be less important, the complex being high spin, and the pattern of deviations is different from that of the bis(imidazole) adduct. Electronic effects associated with porphyrin doming in the five-coordinate complex have been suggested. In the OEiBC core-size plots, however, neither the bis(imidazole) nor the mono(1,2-dimethylimidazole) adduct shows significant deviations (Figure 10). For bis(imidazole)–Fe^{II}OEC, the deviations were found to be less pronounced than for OEP.[31] Thus, there appears to be a trend from porphyrin to chlorin to isobacteriochlorin of diminished back-bonding in the low-spin bis(imidazole) adduct. Again, two possible reasons for this behavior can be advanced: (1) Pyrrole reduction should raise the energy of the e_g^* orbitals (since the size of the π-delocalization pathway is decreased). The interactions with the filled Fe d_π orbital would thereby diminish. (2) Ruffling should increase with pyrrole reduction because of the relatively small size of the low-spin Fe(II) ion, and the e_g^* orbital may become misaligned with respect to the d_π orbital. The absence of iBC core-size deviations for the 1,2-dimethylimidazole adduct suggests that these factors may be important for the five-coordinate high-spin complex as well.

The core-size correlations are not as useful for iBC's as for porphyrins because of the difficulty of assigning the numerous bands reliably. As seen in Figure 9, the intensity pattern is somewhat variable and the band correspondences are not immediately obvious, even with the help of polarization data. The two highest frequency bands, ν_{10} (ap) and ν_{37a} (p), are readily recognized, however. They can serve as indicators of spin state, as was suggested from a study of sulfite reductase RR spectra.[15] These spectra are reconsidered in the light of the model compound data in the following section.

We remark that there does not appear to be a reliable iBC oxidation state marker, a role filled by ν_4 for iron porphyrins. As noted in the assignment section, there are three polarized bands in the ν_4 region, and ν_4 itself is rather weak, at least for NiOEiBC. The spectra in Figure 9 show that the intensity distribution among the multiple bands in the 1380-cm^{-1} region is highly variable. In addition to the three polarized bands, a depolarized band is seen at 1394 cm^{-1} in the spectra of the bis(imidazole)–Fe(III) and $(DMSO)_2Fe^{III}$ complexes, and is probably ν_{20} or ν_{40b} (see Table IV). There is no pattern that correlates reliably with oxidation state. The same observation has been made for chlorins.[31]. It seems that the full 4-fold symmetry of porphyrin is required for the expression of the ν_4 oxidation state marker.

5. Siroheme Coordination and Spin State in Sulfite Reductase. RR spectra of the hemoprotein from sulfite reductase have been interpreted[15] in terms of ligation and spin state on the basis of the porphyrin-like behavior of the high-frequency bands. The present study shows that the presumed analogy with porphyrin has a firm foundation, and the new model compound data permit a more definitive interpretation of the SiR spectra. In Figure 11, we compare the highest frequency bands in the RR spectrum of native oxidized hemoprotein, HP^0, known to contain high-spin iron(III) siroheme, with those of the chloride and $(DMSO)_2$ complexes of Fe^{III}OEiBC, as well as the chloride complex of extracted siroheme. It was noted earlier[15] that the HP^0 frequencies are lower than those of the siroheme chloride, and six-coordination was considered as a possible source of this difference. Figure 11 shows that the ν_{10} and ν_{37a} bands of HP^0 are in fact very close

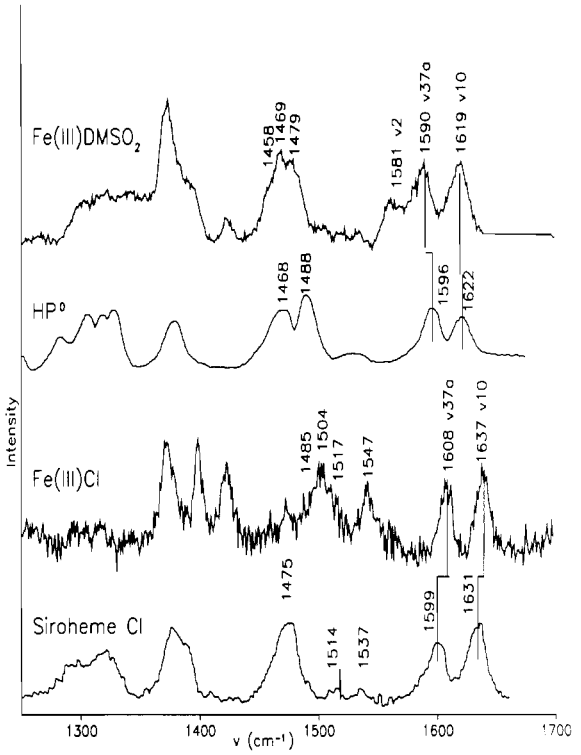

Figure 11. Comparison of the 406.7-nm-excited RR spectra of the $(DMSO)_2$ and chloride complexes of Fe^{III}OEiBC with those of sulfite reductase hemoprotein native (oxidized) form, HP^0, and of siroheme extracted in acetone/HCl. The latter two spectra are redrawn from ref 15.

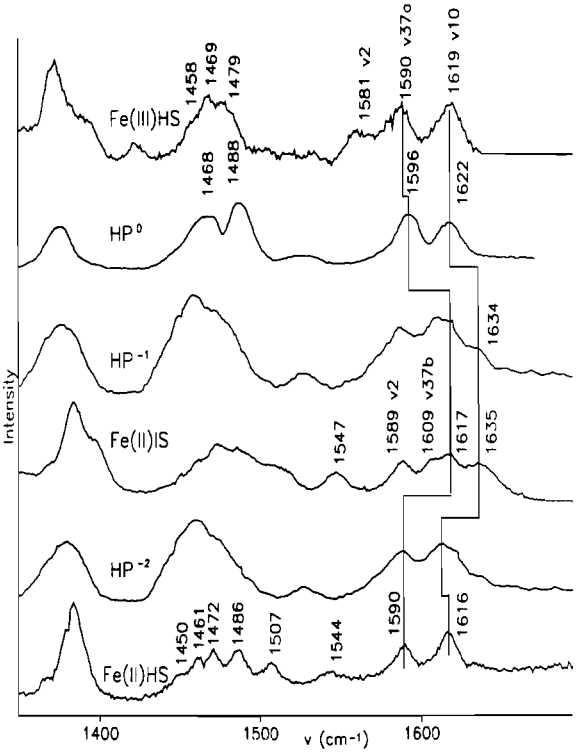

Figure 12. Comparison of 406.7-nm-excited spectra of $[(DMSO)_2Fe^{III}OEiBC]^+$ (labeled $Fe^{III}HS$) Fe^{II}OEiBC (labeled $Fe^{II}IS$), and (1,2-DiMeIm)Fe^{II}OEiBC (labeled $Fe^{II}HS$) with those of HP^0, HP^-, and HP^{2-} (redrawn from ref 14), respectively.

to those of the $(DMSO)_2$ complex of Fe^{III}OEiBC. The chloride complex of Fe^{III}OEiBC has frequencies that are somewhat higher than those of siroheme chloride, but the latter are, in turn, higher than those of HP^0, especially ν_{10}. The HP^0 crystal structure[13] shows the siroheme Fe atom bound to a ligand, probably the S

atom of a cysteine side chain, which bridges to the adjacent Fe_4S_4 cluster, but no electron density is resolved on the distal side. It is unclear, however, in view of the limited resolution of the diffraction data, whether this observation excludes a bound distal ligand, perhaps a water molecule. A sixth, weak-field ligand would provide the most straightforward explanation of the RR frequencies, although it cannot be excluded that some other protein influence, perhaps a ruffling distortion, might mimic the effect of a sixth ligand on the band positions.

An important observation of the SiR study was that reduction of HP^0 by two successive electrons did not produce a monotonic change in the RR spectra.[15] Rather an intermediate spectrum was detected upon addition of one electron, in which the highest frequency band was higher than in either HP^0 or HP^{2-}. This behavior was interpreted as resulting from the formation of low- or intermediate-spin iron(II) siroheme in the intermediate HP^-, which was then converted to high-spin iron(II) siroheme on addition of a second electron, which reduces the Fe_4S_4 cluster. Since the Mössbauer parameters are inconsistent with low-spin iron(II) siroheme in HP^-, an intermediate spin state was inferred. Intermediate-spin Fe(II) results from a weak or absent axial ligand field. It was suggested that reduction of the Fe(III) in HP^0 weakens or breaks the bond to the bridging ligand, presumably cysteine, leaving intermediate-spin Fe(II). Subsequent reduction of the Fe_4S_4 cluster reforms and/or strengthens the bond to the siroheme Fe(II) because of the additional negative charge on the bridging ligand, producing five-coordinate high-spin Fe(II). Figure 12 strengthens this interpretation by showing that the high-frequency RR spectra of all three oxidation levels, HP^0, HP^-, and HP^{2-}, are accurately modeled by the appropriate OEiBC complex, $(DMSO)_2Fe^{III}$, four-coordinate Fe(II), and 1,2-dimethylimidazole–Fe(II), respectively. The close match of HP^- with the intermediate-spin Fe(II) is especially important in confirming the weakening of the axial siroheme bond to the cluster-bound ligand, an interaction that may play an important role in the mechanism of the concerted six-electron reduction of sulfite by SiR.

Acknowledgment. This work was supported by a grant to T.G.S. from the U.S. Department of Energy (DE-FG02-88ER13876) and by grants to S.H.S. from the National Science Foundation (CHE-8805788) and from the donors of the Petroleum Research Fund, administered by the American Chemical Society.

Contribution from the Department of Chemistry, State University of New York, Stony Brook, New York 11794

Redox Reactions of Mixed-Valence Complexes: Kinetic and Thermodynamic Considerations in the (μ-Pyrazine)((ethylenediaminetetraacetato)ruthenato)pentaammineruthenium Ru^{II},Ru^{II}, Ru^{II},Ru^{III}, and Ru^{III},Ru^{III} Systems

M. S. Ram and Albert Haim*

Received April 3, 1990

The oxidation of the mixed-valence compound M in the title (Ru^{III}(EDTA), $Ru^{II}(NH_3)_5$) by peroxydisulfate proceeds according to the rate law $(a + b[S_2O_8^{2-}])[M]$. The peroxydisulfate-independent term corresponds to slow dissociation of M (to form $Ru^{II}(NH_3)_5pz^{2+}$ (pz = pyrazine) and $Ru^{III}(EDTA)OH_2^-$ (EDTA = ethylenediaminetetraacetate)) and is followed by the rapid reaction of $Ru^{II}(NH_3)_5pz^{2+}$ with peroxydisulfate. The peroxydisulfate-dependent term corresponds to direct reaction between M and $S_2O_8^{2-}$. The reduced form (II, II) of the compound in the title, R, reacts with peroxydisulfate according to biphasic kinetics. The first phase corresponds to oxidation of R to M, and the second phase is the reaction of M with $S_2O_8^{2-}$. On the basis of reactivity patterns for the peroxydisulfate oxidation of pyrazine complexes of $Ru^{II}(NH_3)_5^{2+}$ and of $Ru^{II}(EDTA)^{2-}$, it is suggested that oxidation of R yields, as the primary product of the reaction, $(NH_3)_5Ru^{III}pzRu^{II}(EDTA)^+$, the electronic isomer of the title compound M, which then undergoes rapid intramolecular electron transfer to produce the stable isomer M. The thermodynamic stability of M toward disproportionation, electronic isomerization, and dissociation is discussed on the basis of electronic, electrostatic, and metal dπ–ligand π^* bonding factors.

In the past few years, several research groups have synthesized and studied the electrochemical and spectroscopic properties of mixed-valence transition-metal complexes.[1-4] Our contributions to this subject have emphasized the redox reactivities of hetero- and homobinuclear mixed-valence complexes and their corresponding isovalent states.[5-8] In a continuation of this work, we now focus our attention on the title compound, the pyrazine-bridged heterobinuclear complex M, a class II (trapped-valence)

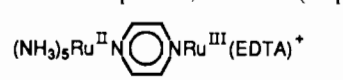

M

mixed-valence compound. (EDTA represents pentadentate ethylenediaminetetraacetate.)[9] The reactions of M with one- and two-electron reagents are reported in the present work. For comparison purposes, we also report some redox reactions of the mononuclear complex $Ru^{II}(EDTA)pz^{2-}$ (pz is pyrazine) and of the completely reduced complex R. In fact, the results obtained with the latter complex proved to be the most interesting.

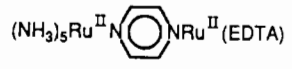

R

Experimental Section

Materials. $Ru^{III}(HEDTA)H_2O{\cdot}4H_2O$ was prepared according to the literature procedure.[10] Trifluoromethanesulfonic acid was purified by distillation under reduced pressure. Lithium trifluoromethanesulfonate was prepared by neutralization of lithium carbonate with CF_3SO_3H. Potassium peroxydisulfate was recrystallized from hot water. House-distilled water was passed through a Barnstead ion-exchange deminer-alizer and then was distilled in a modified, all-glass Corning Model Ag-1b

(1) Creutz, C. *Prog. Inorg. Chem.* **1981**, *30*, 1.
(2) Lay, P. A.; Magnuson, R. H.; Taube, H. *Inorg. Chem.* **1988**, *27*, 2364.
(3) Stebler, A.; Ammeter, J. H.; Furholz, U.; Ludi, A. *Inorg. Chem.* **1984**, *23*, 2764.
(4) Geselowitz, D. A.; Kutner, W.; Meyer, T. J. *Inorg. Chem.* **1986**, *25*, 2015.
(5) Yeh, A.; Haim, A. *J. Am. Chem. Soc.* **1985**, *107*, 369.
(6) Furholz, U.; Haim, A. *J. Phys. Chem.* **1986**, *90*, 3686.
(7) Furholz, U.; Haim, A. *Inorg. Chem.* **1987**, *26*, 3243.
(8) Burewicz, A.; Haim, A. *Inorg. Chem.* **1988**, *27*, 1611.
(9) Creutz, C.; Kroger, P.; Matsubara, T.; Netzel, T. L.; Sutin, N. *J. Am. Chem. Soc.* **1979**, *101*, 5542.
(10) Mukaida, M.; Okuno, H.; Ishimori, T. *Nippon Kagaku Zasshi* **1965**, *86*, 589.

0020-1669/91/1330-1319$02.50/0